nature materials

LETTERS

https://doi.org/10.1038/s41563-019-0584-0

Quantum de-trapping and transport of heavy defects in tungsten

Kazuto Arakawa[1*], Mihai-Cosmin Marinica[2], Steven Fitzgerald[3], Laurent Proville[2], Duc Nguyen-Manh[4], Sergei L. Dudarev[4], Pui-Wai Ma[4], Thomas D. Swinburne[5], Alexandra M. Goryaeva[2], Tetsuya Yamada[6], Takafumi Amino[7], Shigeo Arai[8], Yuta Yamamoto[8], Kimitaka Higuchi[8], Nobuo Tanaka[8], Hidehiro Yasuda[9], Tetsuya Yasuda[9] and Hirotaro Mori[9]

The diffusion of defects in crystalline materials[1] controls macroscopic behaviour of a wide range of processes, including alloying, precipitation, phase transformation and creep[2]. In real materials, intrinsic defects are unavoidably bound to static trapping centres such as impurity atoms, meaning that their diffusion is dominated by de-trapping processes. It is generally believed that de-trapping occurs only by thermal activation. Here, we report the direct observation of the quantum de-trapping of defects below around one-third of the Debye temperature. We successfully monitored the de-trapping and migration of self-interstitial atom clusters, strongly trapped by impurity atoms in tungsten, by triggering de-trapping out of equilibrium at cryogenic temperatures, using high-energy electron irradiation and in situ transmission electron microscopy. The quantum-assisted de-trapping leads to low-temperature diffusion rates orders of magnitude higher than a naive classical estimate suggests. Our analysis shows that this phenomenon is generic to any crystalline material.

Under high-energy irradiation (or extreme mechanical deformation), atoms in a crystal can be displaced substantially from their lattice positions, forming vacancy and self-interstitial atom (SIA) defects. These are ultimately responsible for severe degradation of the mechanical properties of materials, such as hardening, swelling and embrittlement[3]. Understanding the basic mechanisms controlling the formation and diffusion of defects[4–6] is critical for the development of future next-generation energy systems.

In the field of material science, to the best of our knowledge, all the observed migration processes of species heavier than H or He[7,8] have been interpreted as resulting from thermal activation characterized by the Arrhenius rate[9] or phonon dragging[10,11]. No apparent quantum effects have been detected[12], although they have been theoretically considered for SIAs[13–15] and screw dislocations[16]. Quantum effects have also been observed on metal surfaces[17]. We focus here on the low temperature diffusion of SIA clusters in tungsten as a model for crystal defects in heavy-atom systems.

The lowest-energy SIA configuration in tungsten (and other non-magnetic body-centred-cubic (bcc) transition metals) is a ⟨111⟩ crowdion, in which atomic displacements are confined almost entirely to a ⟨111⟩ string containing an extra atom. The defect is delocalized: it involves many more than one atom, as the displacement field is spread down the string, resulting in very low barriers to translation (known as Peierls barriers, see Supplementary Discussion 1a and Extended Data Fig. 1). Hence crowdions perform one-dimensional diffusion along their axis with a low (meV scale) activation energy[10,18,19]. Similar to single crowdions, SIA clusters in the form of $\mathbf{b} = \frac{1}{2}\langle 111\rangle$ dislocation loops undergo one-dimensional glide diffusion in the direction of the Burgers' vector **b**. This phenomenon has been studied using classical molecular dynamics simulations[20–24] and transmission electron microscopy (TEM)[5,25] for α-iron and other metals and alloys.

According to molecular dynamics studies, the activation energy (Peierls barrier) for cluster diffusion is less than 0.1 eV (ref. [20,22]), meaning they are thermally mobile even at very low temperatures. In any real material, however, impurity atoms (mainly carbon and nitrogen) act as traps by binding to the clusters. Vacancies (expected at high density under irradiation) will mutually annihilate with SIAs at the cluster boundary.

Previous studies, using resistivity recovery and internal friction experiments[9], have shown that low-temperature cluster migration in tungsten (and other bcc metals) is strongly influenced by the concentration of impurity atoms[26–28].

These traps are deep enough (~1 eV, see Supplementary Discussion 1b and Extended Data Fig. 2) to prevent TEM observation of the clusters' thermal escape and subsequent motion on experimental timescales, even at 300 K, and they remain immobile. To overcome this, we used the electron beam in transmission electron microscopes such as a high-voltage electron microscope to enhance the vacancy mobility and reduce the effective trap depth. In the absence of the electron beam, vacancies are immobile up to 620–900 K (ref. [9]), but in our experiment, the momentum imparted by the incident electrons moves the vacancies up to 100 times per second. The experimental system is shown schematically in Fig. 1, and operates as follows.

First, a high-energy (2,000 keV) electron beam is used to create displacement damage, vacancies and SIAs at 105 K, before ageing at 300 K. This allows the SIA clusters to nucleate and grow to the nanoscale, with impurities bound to their perimeters (where the binding energy is greatest). At these temperatures, the vacancies are

[1]Next Generation TATARA Co-Creation Centre, Organization for Industrial Innovation, Shimane University, Matsue, Japan. [2]DEN-Service de Recherches de Métallurgie Physique, CEA, Université Paris-Saclay, Gif-sur-Yvette, France. [3]Department of Applied Mathematics, University of Leeds, Leeds, UK. [4]CCFE, United Kingdom Atomic Energy Authority, Culham Science Centre, Abingdon, Oxfordshire, UK. [5]CINaM-Aix Marseille Université, CNRS, Marseille, France. [6]Railway, Automotive & Machinery Parts Unit, Osaka Steel Works, Nippon Steel Corporation, Osaka, Japan. [7]Advanced Technology Research Laboratories, Nippon Steel Corporation, Amagasaki, Japan. [8]Institute of Materials and Systems for Sustainability, Nagoya University, Nagoya, Japan. [9]Research Centre for Ultra-High Voltage Electron Microscopy, Osaka University, Ibaraki, Osaka, Japan. *e-mail: arakawa@riko.shimane-u.ac.jp

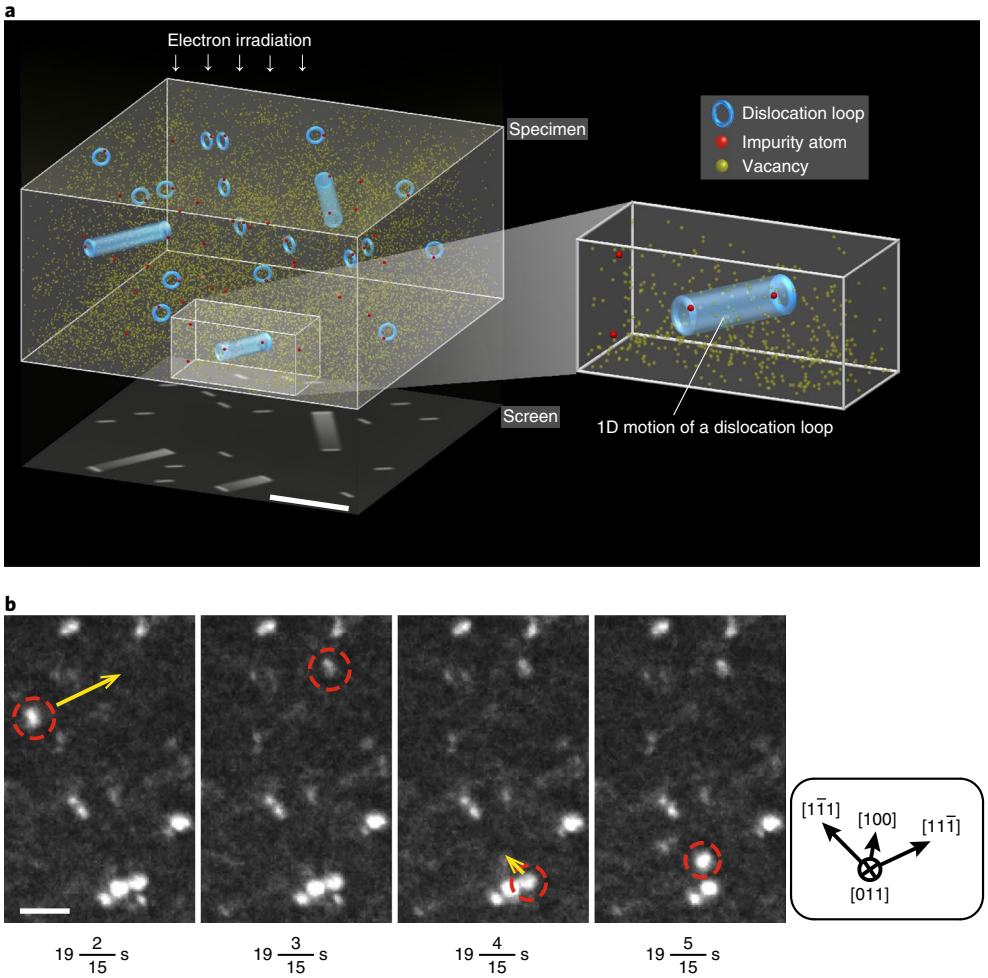

Fig. 1 | One-dimensional SIA cluster motion. a, Experimental setup. In a high-purity tungsten specimen, SIA clusters in the form of nanoscale ½⟨111⟩ dislocation loops are trapped by impurity atoms at their boundary. Scale bar, 20 nm. **b**, High-energy electron irradiation enables clusters to escape, and subsequently undergo fast one-dimensional (1D) glide diffusion before being trapped by other impurity atoms. This one-dimensional motion was monitored simultaneously (acceleration voltage, 1,000 kV; beam intensity, 2×10^{25} m^{-2} s^{-1}; temperature, 260 K, see Supplementary Video 1). The time values denote the time elasped after the start of the high-energy electron irradiation. Circled clusters move in the directions indicated by arrows, parallel to the ⟨111⟩-type cluster Burgers vectors. The clusters hop distances of several nm to a few tens of nm within a single 1/15 s movie frame. Scale bar, 10 nm.

thermally immobile and remain dispersed throughout the sample. A lower energy (100–1,000 keV) electron beam is then turned on to illuminate the sample. The energy of incident electrons is too low to create additional vacancies and SIAs, but high enough to athermally move the existing vacancies (see Methods). Under the beam, the previously trapped clusters begin to move (Fig. 1 and Supplementary Video 1). The principal quantity we monitor is the cluster motion frequency. The precise definition of this quantity, together with its dependence on the experimental irradiation conditions, is given in the Methods and illustrated in Fig. 2. Perhaps the most striking feature of our study is the possibility to resolve the SIA clusters' thermal and quantum-mechanical motion, even in the presence of a flux of vacancies. In the Methods we describe in detail how this is achieved.

The key features of the observed motion of SIA clusters are as follows: first, hops are rare events; that is, the clusters spend far more time being trapped than travelling between traps. Second, clusters sometimes move back and forth between fixed points in the sample. Third, clusters are observed to shrink under the beam. Fourth, motion frequency depends strongly on temperature. The first and second key features tell us that the clusters are escaping from the impurity traps, moving quickly through the lattice before being subsequently trapped again. The third key feature tells us how this occurs: the radiation-mobilized vacancies move through the crystal, attracted to the areas of highly compressive strain at the cluster boundaries. Here, they annihilate with the SIAs at the cluster boundaries, reducing the size of the cluster and increasing the separation between the impurity atom and the cluster boundary. The impurity-cluster interaction is strong but short-ranged (see Supplementary Discussion 1b and Extended Data Fig. 2), and rapidly vanishes over only a few lattice spacings, so that the traps are now much shallower making cluster escape easier (Fig. 2a–c). We now turn to the fourth key feature, the temperature dependence, which demonstrates that the low-temperature escapes are quantum mechanical in nature. It is noted that, for this purpose, we set up the experimental system so that the cluster escapes by the direct electron collision with a cluster itself[29] or the impurity that traps the cluster[30] can be neglected (Methods).

Figure 3 is an Arrhenius plot showing the logarithm of the motion frequency versus inverse temperature. Hops due to thermal escape from potential wells of depth $\Delta V \gg k_B T$ (where k_B is the Boltzmann constant and T is temperature) have a characteristic rate $\propto \exp(-\Delta V/k_B T)$, corresponding to a straight line on an Arrhenius plot. This appears to be the case at higher temperatures

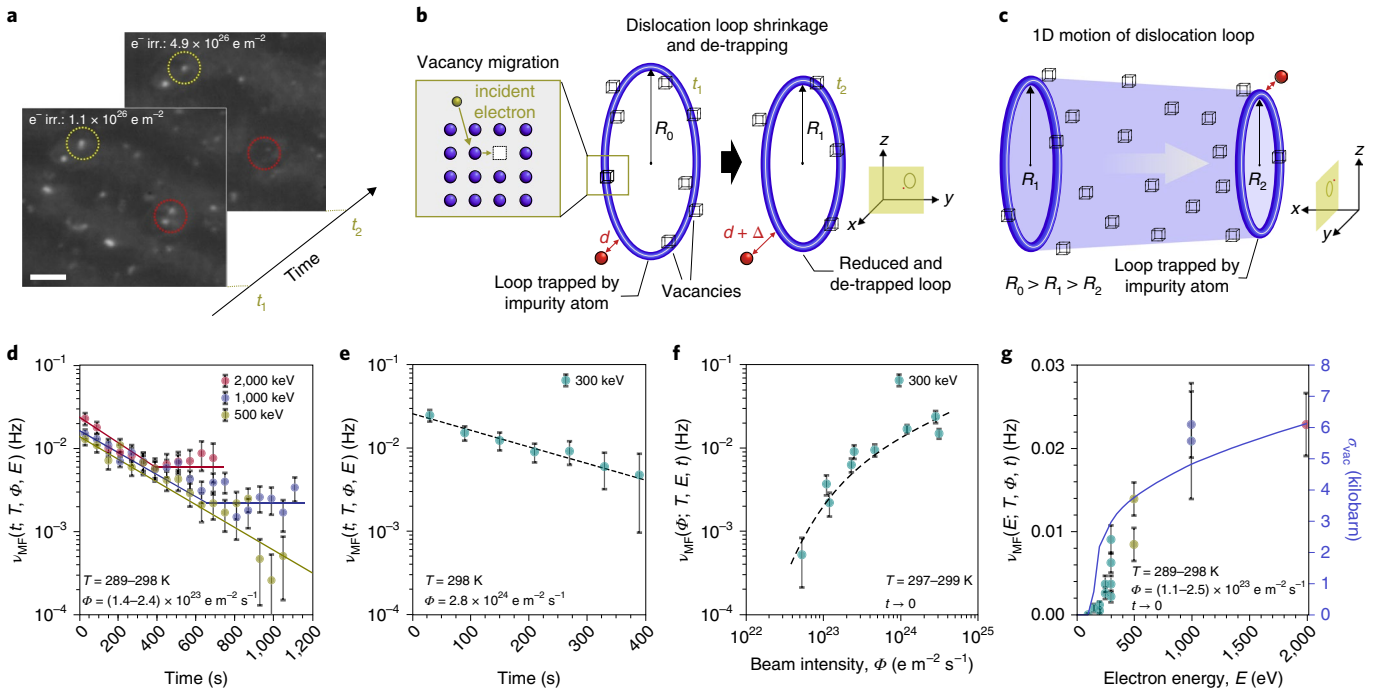

Fig. 2 | Characterization of the motion frequency of SIA cluster de-trapping. a, SIA cluster (dislocation loop) shrinking under the beam (acceleration voltage, 300 kV; beam intensity, 3.1×10^{24} m^{-2} s^{-1}; temperature, 299 K). Vacancies in tungsten are thermally immobile at 299 K, and so the only way the SIA clusters can shrink is via the absorption of radiation-mobilized vacancies. Scale bar, 10 nm. **b**, The clusters escape by increasing the distance between their perimeter and the impurity, from d to $d+\Delta$, as they shrink from radius R_0 at time $t_1 \rightarrow R_1 < R_0$ at time t_2. This reduces the binding energy (see Supplementary Discussion 1) **c**, Stop-and-go motion of the loop in the clouds of vacancies and impurities. Once the loop has escaped from the impurity, it migrates until it is trapped by another impurity. During this macro-jump, over many Peierls barriers, the loop sweeps through the surrounding vacancy clouds, decreasing its effective radius to $R_2 < R_1$. **d**,**e**, Motion frequency decaying exponentially with time under irradiation, which corresponds to the indirect mechanism (see Methods). Plateaus are reached when the supply of vacancies local to the clusters is exhausted by annihilation, and the direct mechanism takes over (see Methods). **f**, Motion frequency increasing with beam intensity (time 0–60 s). **g**, Motion frequency versus beam energy and cross section for radiation-induced vacancy migration (time 0–60 s) (see Methods).

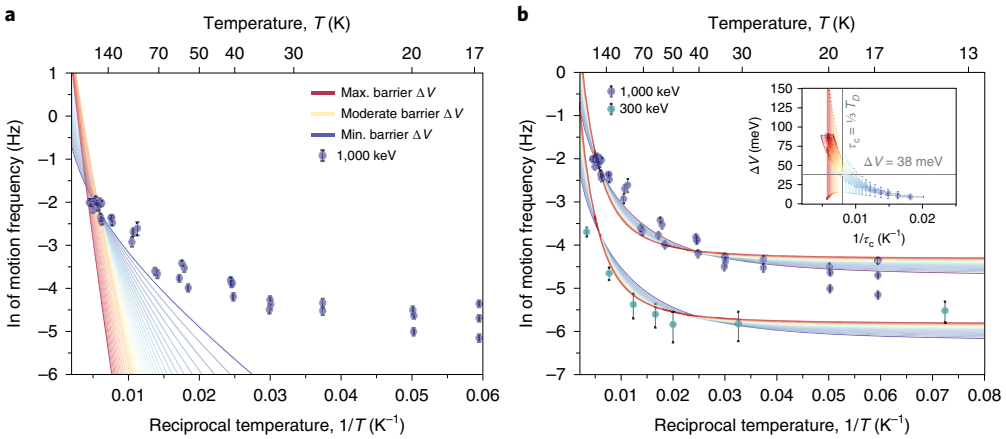

Fig. 3 | Motion frequency of SIA cluster de-trapping versus temperature. Data points show measured motion frequency versus temperature (data taken in first 60 s of irradiation. Blue points, beam energy 1,000 keV, beam intensity 2×10^{25} m^{-2} s^{-1}; green points, beam energy 300 keV, beam intensity $(2\text{–}4)\times10^{24}$ m^{-2} s^{-1}). Some error bars are too small to be visible. **a**, All possible classical fits of one single dataset, at beam energy of 1,000 keV, for activation barriers between 10 meV (blue) and 90 meV (red). Thin lines between are intermediate values. No classical fit can capture the temperature dependence. **b**, As **a**, but using quantum-mechanical rate function. Both 1,000 and 300 keV datasets were fitted simultaneously, with a single parameter to account for the ratio of the two (we obtained a value of 4.52 for the ratio, consistent with Fig. 2g; see Methods). Inset, fitted correlation between activation barrier and critical temperature τ_c (see text and Methods), with corresponding error bars. The value of the effective activation barrier at $\tau_c = \frac{1}{3}T_D$ is 38 meV.

$T \geq 50$ K and the slope suggests that ΔV is higher than 10 meV. As temperature is reduced, $17\text{ K} \leq T \leq 50\text{ K}$, the slope flattens as the de-trapping mechanism changes from classical thermal escape to temperature-independent quantum-mechanical diffusion.

The measured rates result from three independent processes: the athermal radiation-driven vacancy migration under the beam (rate Γ_{vac}), the fluctuation-driven escape of the cluster from the trap (depth ΔV_{trap}, rate Γ_{trap}), and finally the traversal

of the Peierls barrier intrinsic to the crystal (depth ΔV_P, rate Γ_P) (see Methods).

Figure 3a shows attempted classical fits for all barriers 10 meV $\leq \Delta V = \Delta V_P + \Delta V_{trap} \leq 90$ meV. Note that the Peierls traversal rate is non-Arrhenius (since ΔV_P is not more than $k_B T$, see Methods), but no possible classical form for the rate can explain the observed values (we are able to state with confidence that the sample temperatures continue to decrease below 50 K, and are not significantly affected by beam heating—see Supplementary Discussion 2 and Extended Data Fig. 3).

In Fig. 3b, we use a quantum-mechanical form for the escape rate Γ^{QM}, derived from the quantized nature of the crystal phonons (see Methods). These obey Bose–Einstein rather than Boltzmann statistics, and their zero-point fluctuations increase the average energy available for the cluster to overcome the barrier, thus increasing the low-temperature rates, in excellent agreement with experimental observations. Moreover, the same quantum rates simultaneously fit two independent datasets, acquired at two different electron accelerating voltages. This proves that the same fundamentally quantum mechanism explains both datasets.

We are able to obtain acceptable fits for all barriers between 10 and 90 meV. To narrow this down, we consider the critical temperature, τ_c, below which classical physics breaks down (see Methods). This depends on the barrier height: Fig. 2 shows that the 90 meV fit clearly fails below 140 K, whereas the 10 meV one appears reasonable down to around 50 K. τ_c depends on the phonon density of states, and is estimated[31] to be 101 K for pure tungsten (about one-third of the Debye temperature). Fitted values for τ_c are also shown in Fig. 3, and the value of 101 K is consistent with a barrier height of 30–44 meV. We note that the resistivity recovery and internal friction experiments correspond to a barrier height of 15–60 meV (refs. [9,26–28]).

Other manifestations of quantum behaviour are in principle possible, in particular the deep tunnelling of the entire cluster. However, fitting the data to this functional form requires unrealistic values for the cluster's effective mass (see Methods), and we conclude that, over the range of temperatures probed by our experiments, quantized phonons facilitating the clusters' escape from traps that are 30–44 meV deep provide the optimal explanation of the data.

In this study we have performed a direct investigation of cryogenic defect diffusion using in situ TEM. Our unique experimental system allowed us to manipulate the effective potential wells encountered by SIA clusters, reducing their depth until we could probe the quantum-mechanical nature of their de-trapping. The quantum transport becomes dominant below around one-third of the Debye temperature. Moreover, the observed behaviour derives from quantized phonons, which drive the stochastic fluctuations of objects that are themselves too heavy to tunnel non-neglibly. This probably affects the low-temperature transport of defects in many crystalline materials. Our results also demonstrate the importance of quantum effects for low-temperature defect evolution even in heavy-atom systems.

Online content

Any methods, additional references, Nature Research reporting summaries, source data, extended data, supplementary information, acknowledgements, peer review information; details of author contributions and competing interests; and statements of data and code availability are available at https://doi.org/10.1038/s41563-019-0584-0.

Received: 10 August 2017; Accepted: 11 December 2019;
Published online: 27 January 2020

References

1. Mehrer, H. *Diffusion in Solids* Vol. 155 (Springer, 2007).
2. Gupta, D. *Diffusion Processes in Advanced Technological Materials* (William Andrew Inc., 2005).
3. Was, G. S. *Fundamentals of Radiation Materials Science* (Springer, 2007).
4. Fu, C.-C., Torre, J. D., Willaime, F., Bocquet, J.-L. & Barbu, A. Multiscale modelling of defect kinetics in irradiated iron. *Nat. Mater.* **4**, 68–74 (2005).
5. Arakawa, K. et al. Observation of the one-dimensional diffusion of nanometer-sized dislocation loops. *Science* **318**, 956–959 (2007).
6. Bai, X.-M., Voter, A. F., Hoagland, R. G., Nastasi, M. & Uberuaga, B. P. Efficient annealing of radiation damage near grain boundaries via interstitial emission. *Science* **327**, 1631–1634 (2010).
7. Kadono, R. et al. Quantum diffusion of positive muons in copper. *Phys. Rev. B.* **39**, 23–41 (1989).
8. Sundell, P. G. & Wahnström, G. Activation energies for quantum diffusion of hydrogen in metals and on metal surfaces using delocalized nuclei within the density-functional theory. *Phys. Rev. Lett.* **92**, 155901 (2004).
9. Ehrhart, P., Jung, P., Schultz, H. & Ullmaier, H. Atomic Defects in Metals 25 (Springer-Verlag, 1991).
10. Derlet, P. M., Nguyen-Manh, D. & Dudarev, S. L. Multiscale modeling of crowdion and vacancy defects in body-centered-cubic transition metals. *Phys. Rev. B.* **76**, 054107 (2007).
11. Swinburne, T. D., Dudarev, S. L. & Sutton, A. P. Classical mobility of highly mobile crystal defects. *Phys. Rev. Lett.* **113**, 215501 (2014).
12. Wollenberger, H. J. in *Physical Metallurgy, Part II* (eds R. W. Chan & P. Haasen) 1139 (North Holland Physics Publishing, 1983).
13. Pushkarov, D. I. Quantum theory of crowdions at low temperatures. *Soviet Journal of Experimental and Theoretical Physics* **37**, 322–325 (1973).
14. Flynn, C. P. Resonance mode hopping and the stage I annealing of metals. *Thin Solid Films* **25**, 37–43 (1975).
15. Swinburne, T. D., Ma, P.-W. & Dudarev, S. L. Low temperature diffusivity of self-interstitial defects in tungsten. *N. J. Phys.* **19**, 073024 (2017).
16. Proville, L., Rodney, D. & Marinica, M.-C. Quantum effect on thermally activated glide of dislocations. *Nat. Mater.* **11**, 845–849 (2012).
17. Ohresser, P. et al. Surface diffusion of Cr adatoms on Au(111) by quantum tunneling. *Phys. Rev. Lett.* **95**, 195901 (2005).
18. Fitzgerald, S. P. & Nguyen-Manh, D. Peierls potential for crowdions in the bcc transition metals. *Phys. Rev. Lett.* **101**, 115504 (2008).
19. Amino, T., Arakawa, K. & Mori, H. Detection of one-dimensional migration of single self-interstitial atoms in tungsten using high-voltage electron microscopy. *Sci. Rep.* **6**, 26099 (2016).
20. Wirth, B. D., Odette, G. R., Maroudas, D. & Lucas, G. E. Dislocation loop structure, energy and mobility of self-interstitial atom clusters in bcc iron. *J. Nucl. Mater.* **276**, 33–40 (2000).
21. Marian, J. et al. Dynamics of self-interstitial cluster migration in pure α-Fe and Fe-Cu alloys. *Phys. Rev. B.* **65**, 144102 (2002).
22. Osetsky, Y. N., Bacon, D. J., Serra, A., Singh, B. N. & Golubov, S. I. One-dimensional atomic transport by clusters of self-interstitial atoms in iron and copper. *Philos. Mag.* **83**, 61–91 (2003).
23. Dudarev, S. L. The non-Arrhenius migration of interstitial defects in bcc transition metals. *Comptes Rendus Phys.* **9**, 409–417 (2008).
24. Swinburne, T. D., Dudarev, S. L., Fitzgerald, S. P., Gilbert, M. R. & Sutton, A. P. Theory and simulation of the diffusion of kinks on dislocations in bcc metals. *Phys. Rev. B.* **87**, 064108 (2013).
25. Arakawa, K., Amino, T. & Mori, H. One-dimensional glide motion of 'naked' 1/2<111> prismatic dislocation loops in iron. *ISIJ Int.* **54**, 2421–2424 (2014).
26. Dausinger, F. & Schultz, H. Long-range migration of self-interstitial atoms in tungsten. *Phys. Rev. Lett.* **35**, 1773–1775 (1975).
27. Dausinger, F. Die Tieftemperaturerholung in elektronenbestrahltem Wolfram. *Philos. Mag. A* **37**, 819–836 (1978).
28. Mizubayashi, H. & Okuda, S. Elastic after-effect studies of self-interstitials in tungsten after fast neutron irradiation at 5 K. *Radiat. Eff.* **54**, 201–215 (1981).
29. Dudarev, S. L., Derlet, P. M. & Woo, C. H. Driven mobility of self-interstitial defects under electron irradiation. *Nucl. Instrum. Methods Phys. Res. B.* **256**, 253–259 (2007).
30. Satoh, Y., Matsui, H. & Hamaoka, T. Effects of impurities on one-dimensional migration of interstitial clusters in iron under electron irradiation. *Phys. Rev. B.* **77**, 94135 (2008).
31. Ashcroft, N. W. & Mermin, N. D. *Solid State Physics* (Holt, Rinehart and Winston, 1978).

Methods

Specimen preparation. We cut (011) discs from one grain of an ingot of high-purity coarse-grained polycrystalline tungsten (99.9999 mass per cent JX Nippon Mining & Metals Co.; impurity amounts of the ingot are given in ref. [32]). The discs were thinned to 0.1 mm, using spark erosion and mechanical polishing, then perforated at the centre by electropolishing so the periphery of the hole became cross-sectionally wedge-shaped for TEM observations.

Production of SIA clusters. We used high-energy electron irradiation in a high-voltage electron microscope (Hitachi H-3000) to create SIAs and vacancies in the thin foil specimens. The acceleration voltage was 2,000 kV, and a temperature of 105 K was maintained using a liquid-nitrogen-cooled specimen holder (Oxford Instruments). We note that the thermal migration of vacancies is frozen at temperatures below 620–900 K (ref. [9]). The beam flux was $1\times10^{24}\,m^{-2}\,s^{-1}$ and the dose was $4\times10^{25}\,m^{-2}$.

During 2,000-keV electron irradiation, pairs of SIAs and vacancies are produced[33] via knock-on displacement. On the basis of our recent work[19,32], the point defect reactions proceed as follows: most of the highly mobile one-dimensional-moving SIAs react with vacancies, or escape to the foil surface, where they are annihilated. Surviving SIAs bind to impurity atoms and form embryonic SIA clusters, that grow by absorbing other SIAs, and take the form of $\mathbf{b}=\frac{1}{2}\langle111\rangle$ dislocation loops. These clusters are intrinsically highly mobile, yet they are trapped by impurities and remain stationary. Vacancies that do not react with SIAs accumulate throughout the irradiated area of the specimen.

Using TEM, the average size and density of the SIA clusters formed under the above conditions were found to be approximately 3–4 nm and $4\times10^{22}\,m^{-3}$, respectively. Accumulated vacancies are not visible in the TEM. After the irradiation, the specimen was aged at approximately 300 K. This allows the clusters trapped by weak impurity atoms with shallow potential wells to thermally escape and move, leading to coalescence with other clusters[34], escape to the specimen surfaces, or to trapping by stronger impurities with deeper wells. However, even after ageing for several months, we did not see any significant change in the cluster density, demonstrating that thermal escape of SIA clusters from the deeper wells hardly occurs even at 300 K.

TEM observation of the one-dimensional motion of SIA clusters in response to high-energy electron irradiation. We then used the electron beam to induce the vacancy mobility, with acceleration voltages of 100, 150, 300, 500 (Hitachi H-9000UHV), 1,000 and 2,000 kV (H-3000)—all except 2,000 kV are below the threshold for point defect generation in tungsten[33]. Additional very intense irradiations were carried out at 1,000 kV using a JEOL JEM 1000K RS. Beam fluxes ranged from 5×10^{22} to $2\times10^{25}\,m^{-2}\,s^{-1}$, and temperatures ranged from 17–300 K (where no thermal migration of vacancies takes place[9]). We achieved these temperatures using liquid-helium-cooled specimen holders (Oxford Instruments), in which the temperature is measured with a thermocouple attached to the specimen mount, so the measured temperature is the average over the whole specimen.

The specimen thickness ranged from 50 to 70 nm (measured using equal-thickness fringes[35]). The observations were carried out using the weak-beam dark-field technique[36] with a reflection of $\mathbf{g}=200$. Under this condition, all SIA clusters in the form of prismatic dislocation loops with a $\mathbf{b}=\frac{1}{2}\langle111\rangle$ type Burgers vector and a diameter greater than approximately 2 nm were imaged. The dynamic response of the clusters was monitored and recorded with charge-coupled devices having frame rates of 30 frames per second for H-9000UHV and H-3000, and 15 frames per second for JEM 1000K RS.

We define the motion frequency of the clusters as the ratio of the number of cluster hops observed per unit time divided by the number of observable clusters; that is, the average motion frequency of individual SIA clusters.

Motion frequency and the ballistic and kinetic rates of SIA clusters. Our experiments measure the average motion frequency of SIA clusters under electron irradiation as simultaneously observed in the transmission electron microscopes. The average motion frequency at irradiation (observation) time t is defined as $\nu_{MF}(t)=n_m/(n\Delta t)$: the ratio of the number of clusters that move (n_m) divided by the total number of observed clusters (n) in the observation duration Δt.

The measured rates ν_{MF} are the combined results of motion induced directly by the irradiation, and stochastic motion induced by the underlying phonon bath. Consequently, the motion frequency is impacted by irradiation conditions, in particular the electron beam flux Φ and energy E. The temperature T also influences the experimental observations through the phonon bath, meaning that the motion frequency is a function defined on a four-dimensional space $\nu_{MF}(t, T, \Phi, E)$. Figure 3 illustrates the temperature dependence and Fig. 2d–g shows the behaviour of the motion frequency with respect to the other variables. Here, we derive an expression for the motion frequency in the context of the experiments.

Detailed experimental analysis suggests that the shrinkage of the clusters (Fig. 2a) originates from irradiation-induced vacancy motion (Fig. 2b). Since the impurities are immobile, the erosion of the clusters by the vacancies increases the distance between them and the impurities, which leads to the de-trapping of the clusters from the impurities. We call this the indirect de-trapping mechanism. Since it depends on the radiation-mobilized vacancies eroding the SIA clusters, the cluster motion frequency is proportional to the vacancy concentration, c_V. These vacancies are absorbed by the clusters, and other sinks such as the specimen surface, at a rate proportional to the concentration of vacancies itself: $\dot{c}_V \propto -c_V$. As long as no new Frenkel pairs are created, this leads to an exponential decay of vacancy concentration as a function of time, and the corresponding variation of the cluster motion frequency. This is precisely what we find in Fig. 2c,d, in the limit of short observation time.

In the indirect mechanism, cluster de-trapping is also impacted by the thermal rate at which the clusters escape from the impurities. At a given cluster-impurity separation, d_k, sufficiently large that the trapping energy is low, the thermal escape rate Γ^k_{th} is governed by the cluster-impurity trapping energy ΔV^k_{trap} for that distance (see next section). If we have n_k cluster-impurity sets at given cluster-impurity separation d_k, then the number of clusters that jump within the observation time is $a\,c_V n_k \Gamma^k_{th}\Delta t$. Prefactor a accounts for the effect of the beam flux and energy on the observations.

Since the incident electron energy is high, what we call the direct de-trapping mechanism—direct collision of the electron with a cluster itself[29] or the impurity that traps the cluster[30]—can also release the cluster. The de-trapping rate Γ_d associated with this direct mechanism is independent of temperature and uniform in time, depending only on the concentration of cluster-trapping impurities and the flux and energy of the electrons. The probability of releasing a cluster from an impurity via the direct mechanism is $n\Gamma_d\Delta t$.

Consequently, the measured motion frequency can be written as

$$\nu_{MF}=\frac{n_{indirect}+n_{direct}}{n\,\Delta t}=\frac{\sum_k a c_V n_k \Gamma^k_{th}(T)\Delta t + n\Gamma_d\Delta t}{n\,\Delta t}$$

Or, in a simpler form, if we assume that in the system the initial vacancy density $c_V(0)$ decreases in time with a decay factor α_v:

$$\nu_{MF}\approx\sum_k a\,c_V(0)e^{-\alpha_v t}\frac{\Gamma^k_{th}(T)n_k}{n}+\Gamma_d=e^{-\alpha_v t}\left[\sum_k a c_V(0)\frac{\Gamma^k_{th}(T)n_k}{n}\right]+\Gamma_d$$

This theoretical expression for the motion frequency is fully compatible with all the experimental evidence described in the body of the paper and illustrated in Fig. 2.

First, the experimental observations shown in Fig. 2d,e indicate that the motion frequency decreases exponentially in time, and after several hundred seconds, the frequency's exponential decay becomes a constant plateau. This reflects the local exhaustion of vacancies near the clusters, and the transition to de-trapping by direct electron impacts, through what we term the direct mechanism. The $t\to\infty$ limit corresponds to the frequency of de-trapping events associated with the direct mechanism $\nu_{MF}\to\Gamma_d$. On the other hand, in the limit of $t\to0$.

$$\nu_{MF}(t\to0)=\left[\sum_k a_k c_v(0)\frac{\Gamma^k_{th}(T)n_k}{n}\right]+\Gamma_d\approx\text{const}\times\Gamma^0_{th}(T)+\Gamma_d$$

we have access, up to multiplicative (const) and additive (Γ_d) constants, to the dominant thermal/quantum rate $\Gamma^0_{th}(T)$ on the nature of which, classical or quantum, our study is focused. We note that the higher the beam energy, the greater is the part played by the direct mechanism of de-trapping, and the sooner the hopping rate reaches the asymptotic value. The plateaus are also higher for higher beam energies, reflecting the direct mechanism's expected variation as a function of the incident electron beam energy.

Second, Fig. 2f shows the cluster motion frequency's strong dependence on the beam intensity at 300 kV, clearly illustrating a role the irradiation contributes through the multiplicative constants. Note that no further Frenkel pairs are created if the beam energy is at or below 1,000 kV.

Finally, Fig. 2g shows the electron energy dependence of $\nu_{MF}(t\to0, E)$, together with the athermal radiation-driven vacancy migration rate under the beam Γ_{vac}. The Γ_{vac} value is proportional to the product of beam flux and the cross section for radiation-induced vacancy migration[37],

$$\sigma_{mig}\approx\int_{E^V_{mig}}^{E_{K,max}}\frac{E_K}{E^V_{mig}}\frac{d\sigma}{dE_K}dE_K$$

where E_K is the kinetic energy transferred from an incident electron to a tungsten atom neighbouring a vacancy, E^V_{mig} is the vacancy migration energy (1.78 eV, ref. [38]) and $d\sigma$ is the differential cross section for the electron-tungsten atom collision calculated using the McKinley–Feshbach formula[39]. The high degree of correlation between the two is abundantly clear, providing a further confirmation of the vacancy origin of the indirect mechanism of cluster de-trapping and migration.

A natural question is whether this approach has sufficient accuracy to reveal the classical or quantum nature of the cluster migration rate. The quantity of interest is the logarithm of the motion frequency, which can be written as:

$$\ln\nu_{MF}(t\to0)=\ln\left[\Gamma^0_{th}(T)+\Gamma_d\right]\approx\ln\Gamma^0_{th}(T)+\frac{\Gamma_d}{\Gamma^0_{th}(T)}$$

The second term of the right side is easily estimated from the ratio of asymptotic limits $\nu_{MF}(t\to 0)/\nu_{MF}(t\to\infty)$. This quantity is in the order of 10^{-1} and 10^{-2} at 1,000 keV and 500 keV, respectively, for 289–298 K (Fig. 2d). Also, it is shown to be no higher than 0.2 at 300 keV even at 31 K (Extended Data Fig. 4). This analysis shows that in terms of observed logarithm of $\nu_{MF}(t\to 0)$, the effect of direct de-trapping mechanism is visible at the level after the first or even the second place after the decimal point. Hence, the direct and indirect contributions to the motion frequency can be reliably separated.

We provide the details of the statistical procedure used for measuring ν_{MF}. One specimen involved 1×10^2 areas for 2,000-keV electron irradiation for the SIA cluster production, at maximum. The n value within one area of interest (AOI) centred at a 2,000-keV electron irradiated area was $(1-2)\times10^2$ for $t=0$ s. This n value was the practical upper limit under the lowest TEM magnification enabling the observation of the cluster motion. In the time dependence of $\nu_{MF}(t)$ (Fig. 2d,e and Extended Data Fig. 4), matching symbols correspond to the same AOI, and in the beam flux dependence of $\nu_{MF}(t\to 0, \Phi)$ (Fig. 2f), energy dependence of $\nu_{MF}(t\to 0, E)$ (Fig. 2g) and temperature dependence of ν_{MF} $(t\to 0, T)$ (Fig. 3), individual data points correspond to different AOIs. The error in the ν_{MF} value was evaluated under the assumption that both the distributions of n and n_m for a given AOI independently obey Poisson statistics. Then, the error in a measured ν_{MF} value becomes $\nu_{MF}\sqrt{\frac{1}{n}+\frac{1}{n_m}}$. The datasets for temperature dependence of ν_{MF} $(t\to 0, T)$ with other conditions fixed (Fig. 3) were acquired from the areas belonging to an identical TEM specimen so that the impurity concentration in the measured areas was very similar level.

Diffusion rates in quantum and classical phonon baths. The archetypal problem of a particle traversing a potential barrier has been treated exhaustively; see ref. [40] for a thorough review. For a barrier height $\Delta V \gg k_B T$, the classical escape rate is given by the Arrhenius function $\Gamma_{th}^{cl} = f_{cl}\exp(-\Delta V/k_B T)$, where the classical prefactor f_{cl} can be loosely interpreted as an attempt frequency. As $k_B T$ rises towards ΔV the Arrhenius function breaks down, and the rate transitions to a form linear in the temperature[11,23] (manifested as a sharp steepening on an Arrhenius plot). For barriers $\Delta V \approx k_B T$ or less, the particle migrates stochastically, being slowed only by the dissipative coupling between the particle and the underlying phonon bath. This is quantified by the friction parameter γ, and the rate is proportional to $k_B T/\gamma$ (refs. [11,23,41]). If $\Delta V << k_B T$, the friction can be absorbed into f_{cl}[40,42]. Both standard rate formulae originate from the classical Boltzmann distribution for the phonons. For clusters escaping from traps, the barrier to be overcome is $\Delta V = \Delta V_P + \Delta V_{trap}$, the sum of the Peierls barrier and the critical binding energy of the impurity or vacancy, respectively. Therefore, the diffusion rate is the product of two independent probabilities: the probability related to the free migration of the SIA cluster through the Peierls potential in the absence of a trap, and the escape probability from the trap itself: $\Gamma_{th}^{cl}(T) = \Gamma_P(T)\times\Gamma_{trap}(T)$. $\Delta V_{trap} >> k_B T$, so Γ_{trap} is Arrhenius in the classical limit. Since the Peierls barrier ΔV_P for SIA clusters (also known as ½⟨111⟩ loops) is small, that is of order $k_B T$, the total classical rate becomes:

$$\Gamma_{th}^{cl}(T) = \text{const.}\times k_B T \times \exp\left(-\frac{\Delta V_{trap}}{k_B T}\right) \quad (1)$$

We note that the constant prefactor above can take on a weak temperature dependence in other formulations of the rate; we obtain similar fits in either case and our conclusions are unaffected.

The full quantum-mechanical development is more complicated. Here, the Boltzmann distribution is replaced by either the Bose–Einstein or Fermi–Dirac distribution, for bosons or fermions respectively. For tungsten or impurity atoms the ground state has integer spin and hence obeys Bose–Einstein statistic. A simple way to recover the Bose–Einstein phonon distribution whilst retaining the form of the classical rate formulae is to renormalize the temperature to mimic the true quantum statistics[15,42,43]. Consider a crystal with periodic boundary conditions represented by N atoms in a box. Imposing equality of the classical and quantum energies, the (renormalized, effective) classical temperature and the (true) quantum temperature should be related by the relation:

$$(3N-3)k_B T_c = \int d\omega\, \hbar\omega \left(\rho_{BE}(\omega, T_q) + \frac{1}{2}\right) n(\omega)$$

where T_c and T_q are the (renormalized, effective) classical and (true) quantum temperatures, respectively; $n(\omega)$ is the density of states of the phonon gas, normalized to the number of modes and $\rho_{BE}(\omega,T_q)$ is the Bose–Einstein (BE) distribution function. Therefore, the effective classical temperature is a function of the true quantum temperature $T_c = f(T_q)$.

For temperatures higher than the Debye temperature T_D, $\hbar\omega \ll k_B T$, the energy of one oscillator becomes:

$$\hbar\omega\left(\rho_{BE}(\omega, T_q) + \frac{1}{2}\right) \approx \frac{\hbar\omega}{2} + k_B T_q\left(1 - \frac{\hbar\omega}{2k_B T_q}\right) = k_B T_q$$

and the classical and quantum temperatures are very close. When the (true) quantum temperature T_q tends to 0 K, the effective classical temperature T_c tends to a finite limit, capturing the zero-point energy:

$$(3N-3)k_B T_c = \int d\omega \frac{1}{2}\hbar\omega\, n(\omega)$$

The simple form $T_c = \sqrt{\tau_c^2 + T_q^2}$ satisfies these limits (see Extended Data Fig. 5). Therefore, the quantum rates can be estimated by simply renormalizing the temperature in equation (1) yielding:

$$\Gamma_{th}^{QM}(T) = \text{const.}\times k_B\sqrt{\tau_c^2 + T^2}\times\exp\left(-\frac{\Delta V_{trap}}{k_B\sqrt{\tau_c^2 + T^2}}\right) \quad (2)$$

We also attempted to fit the data with up to three distinct classical barrier escape mechanisms operating simultaneously. Only the quantum rates explain the observed temperature dependence.

Quantum transition state theory rates. For deep tunnelling, we computed the rate by numerically integrating the quantum transition state theory rate expression[42]

$$\Gamma_{th}^{QTST} = (hZ_0)^{-1}\int W(E)e^{-E/k_B T}dE$$

where h is the Planck constant and $W(E)$ is the transfer integral at energy E for the sech-squared impurity interaction potential predicted by the Frenkel Kontorova model (see Supplementary Discussion 1). The data can be fitted with a barrier height of 55 meV, but requires an unrealistically low effective cluster mass of $m_W/200$ (m_W is the mass of one tungsten atom). The remaining parameters (potential width and curvature) are fixed by the Arrhenius limit, which applies to the highest temperature points in the dataset.

Data availability

The data generated and/or analysed within the current study will be made available on reasonable request to the corresponding author.

References

32. Amino, T., Arakawa, K. & Mori, H. Activation energy for long-range migration of self-interstitial atoms in tungsten obtained by direct measurement of radiation-induced point-defect clusters. *Philos. Mag. Lett.* **91**, 86–96 (2011).
33. Maury, F., Biget, M., Vajda, P., Lucasson, A. & Lucasson, P. Frenkel pair creation and stage I recovery in W crystals irradiated near threshold. *Radiat. Eff.* **38**, 53–65 (1978).
34. Arakawa, K., Amino, T. & Mori, H. Direct observation of the coalescence process between nanoscale dislocation loops with different Burgers vectors. *Acta Mater.* **59**, 141–145 (2011).
35. Hirsch, P. B., Howie, A., Nicholson, R. B., Pashley, D. W. & Whelan, M. J. Electron Microscopy of Thin Crystals (Butterworth, 1965).
36. Jenkins, M. L. & Kirk, M. A. Characterization of Radiation Damage by Transmission Electron Microscopy (Institute of Physics, 2001).
37. Kiritani, M. Electron radiation induced diffusion of point defects in metals. *J. Phys. Soc. Jpn* **40**, 1035–1042 (1976).
38. Nguyen-Manh, D., Horsfield, A. P. & Dudarev, S. L. Self-interstitial atom defects in bcc transition metals: group-specific trends. *Phys. Rev. B.* **73**, 020101 (R) (2006).
39. Oen, O. S. *Cross Sections for Atomic Displacements in Solids by Fast Electrons* (Oak Ridge National Laboratory, 1965).
40. Hänggi, P., Talkner, P. & Borkovec, M. Reaction-rate theory: fifty years after Kramers. *Rev. Mod. Phys.* **62**, 251–341 (1990).
41. Dudarev, S. L. Coherent motion of interstitial defects in a crystalline material. *Philos. Mag.* **83**, 3577–3597 (2003).
42. Benderskii, V., Makarov, D. & Wight, C. *Chemical Dynamics at Low Temperature* (Wiley, 1994).
43. Wang, C. Z., Chan, C. T. & Ho, K. M. Tight-binding molecular-dynamics study of phonon anharmonic effects in silicon and diamond. *Phys. Rev. B.* **42**, 11276–11283 (1990).

Acknowledgements

This work was financially supported by JSPS KAKENHI (grant nos. 15H04244 and 18K18951), ImPACT Program of Council for Science, Technology and Innovation (Cabinet Office, Government of Japan), Q-LEAP Program (MEXT: Ministry of Education, Culture, Sports, Science and Technology—Japan), and the Iron and Steel Institute of Japan Research Promotion Grant. Part of this work was supported by the 'Advanced Characterization Nanotechnology Platform, Nanotechnology Platform Programs' of MEXT, at Institute of Materials and Systems for Sustainability (Nanotechnology Open Facilities) in Nagoya University and at Research Centre for Ultra-High Voltage Electron Microscopy (Nanotechnology Open Facilities) in Osaka University and TATARA Nanotechnology Project Centre in Shimane University. M.C.M., L.P. and A.M.G. acknowledge support from the GENCI-(CINES/CCRT) computer centre under grant no. A0070906973. A.M.G. and M.C.M acknowledge the financial

support of the Cross-Disciplinary Program on Numerical Simulation of CEA, the French Alternative Energies and Atomic Energy Commission. S.P.F. acknowledges support from the UK EPSRC, grant no. EP/R005974/1. The work at CCFE has been carried out within the framework of the EUROfusion Consortium and has received funding from the Euratom research and training programme 2019–2020 under grant agreement no. 633053 and funding from the RCUK Energy Programme (grant no. EP/T012250/1). The views and opinions expressed herein do not necessarily reflect those of the European Commission.

Author contributions

K.A., M.C.M. and L.P. designed the study. K.A., T.Y., T.A., S.A., Y.Y., K.H., N.T., H.Y., T.Y. and H.M. performed the experiments. M.C.M., S.F., L.P., D.N.M., A.M.G., S.L.D., P.W.M. and T.D.S. performed the theoretical works. K.A., M.C.M., S.F. and S.L.D. wrote the main draft. All authors discussed the results and commented on the manuscript.

Competing interests

The authors declare no competing interests.

Additional information

Extended data is available for this paper at https://doi.org/10.1038/s41563-019-0584-0.

Supplementary information is available for this paper at https://doi.org/10.1038/s41563-019-0584-0.

Correspondence and requests for materials should be addressed to K.A.

Reprints and permissions information is available at www.nature.com/reprints.

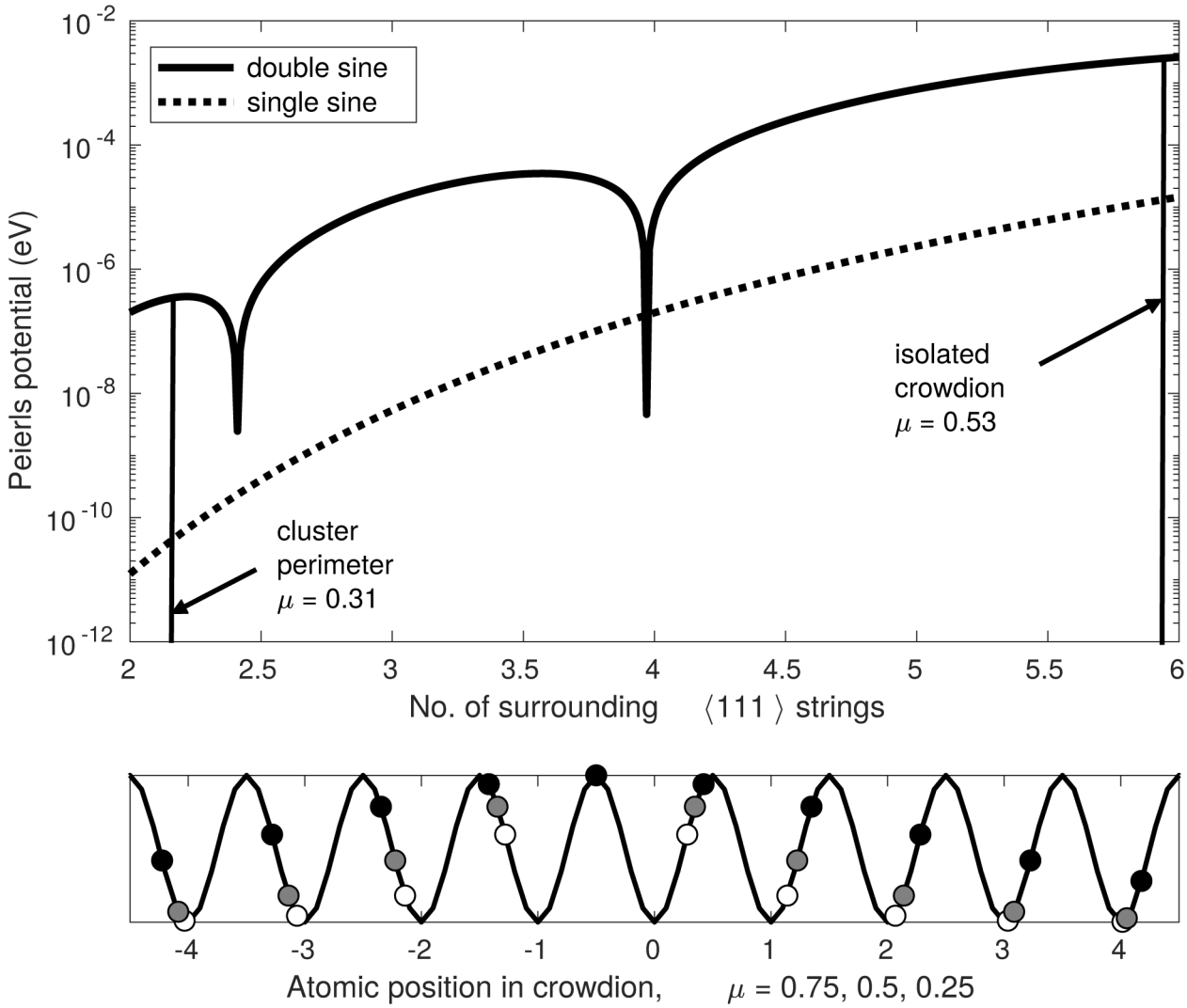

Extended Data Fig. 1 | Suppression of the SIA cluster Peierls potential. Top: suppression of Peierls potential as delocalization increases (and μ decreases). Both the standard single-sine and more accurate double-sine Frenkel-Kontorova models predict a negligibly small barrier for cluster diffusion after escape from the traps. Bottom: atomic positions showing increased delocalization as μ decreases from 0.75 (open circles) through 0.5 (grey circles) to 0.25 (solid circles).

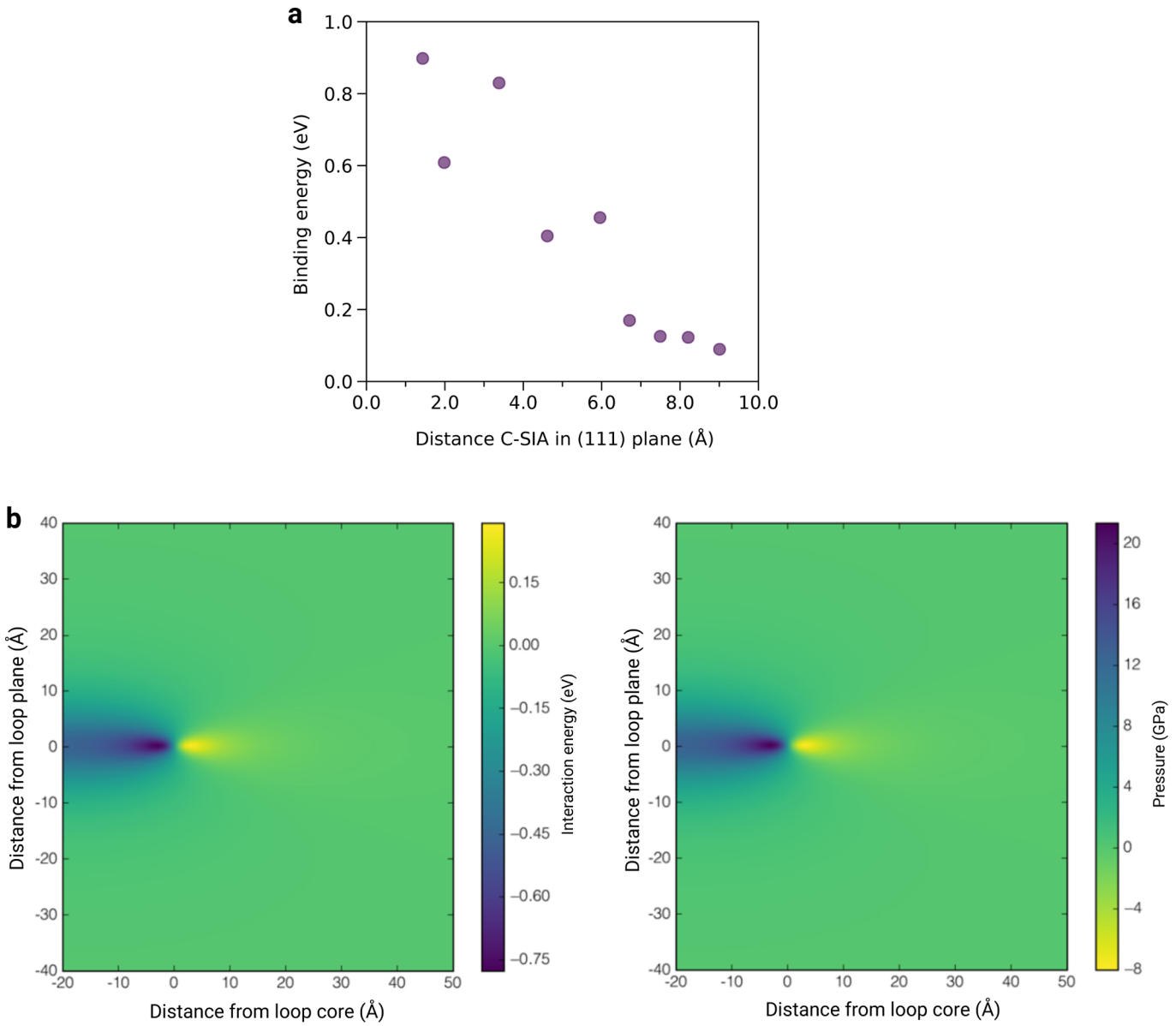

Extended Data Fig. 2 | Calculation of the SIA cluster binding energies. a, DFT calculation of the SIA-carbon binding energy vs. separation in plane transverse to the crowdion axis. **b**, Elastic calculation of the SIA cluster-dilatation centre binding energy (left) and cluster pressure field (right).

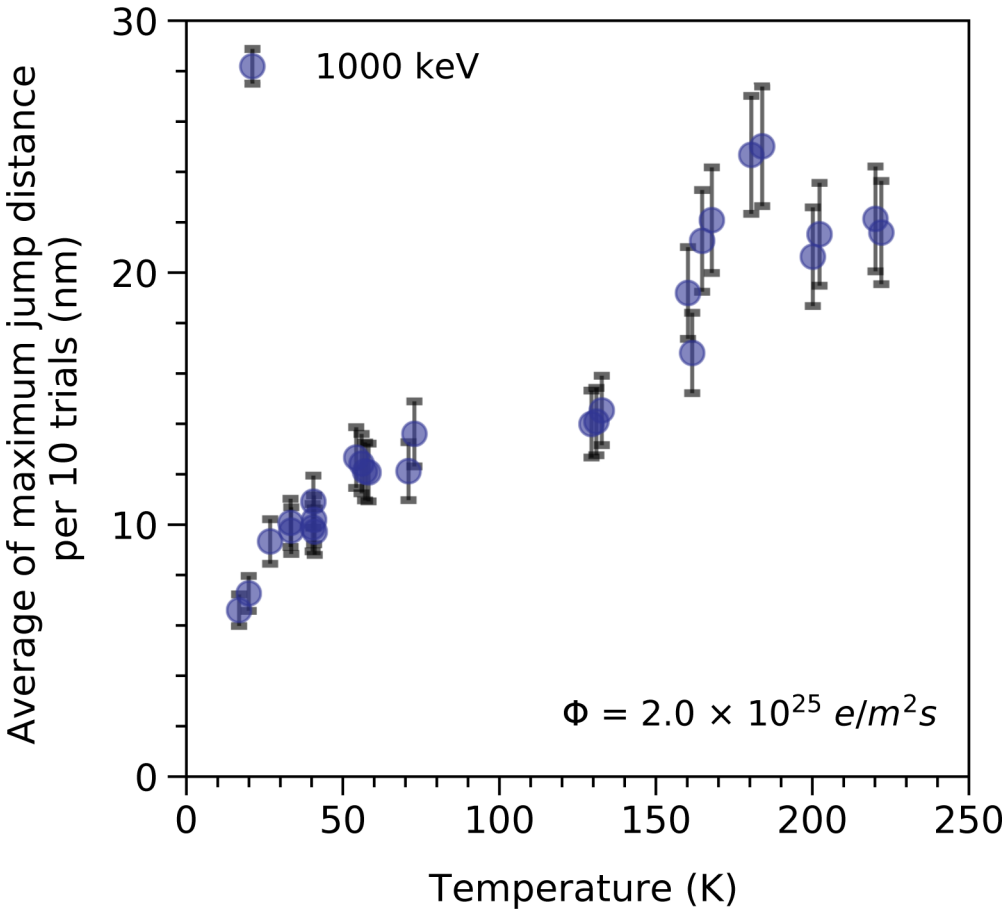

Extended Data Fig. 3 | Average maximum hop distance per 10 hops vs temperature. A range of binding energies exist, corresponding to different cluster-impurity separations. This means more impurities are effective traps at lower temperatures, leading to a reduced hop distance.

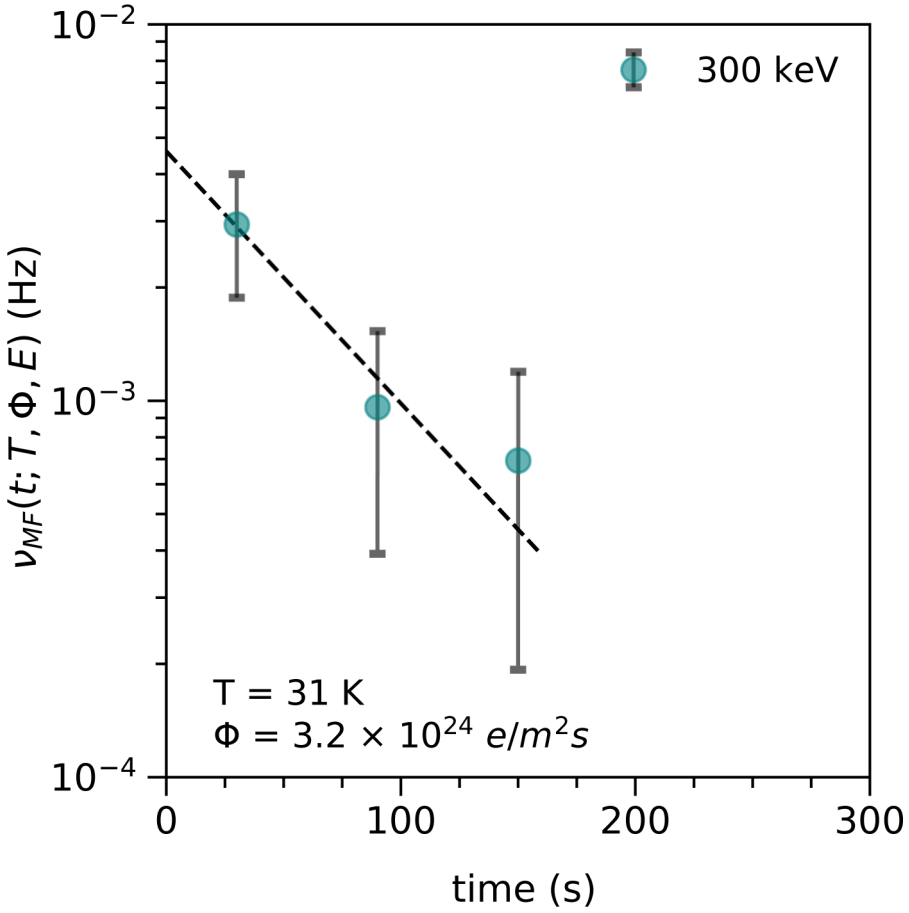

Extended Data Fig. 4 | Motion frequency vs irradiation time at 31 K, with beam energy 300 keV. The decrease in motion frequency, attributed to the depletion of vacancies near the clusters, is still clear, and demonstrates that the direct mechanism (which would induce a motion frequency constant in time) is not wholly responsible for the cluster motion. Indeed, at short times the motion is dominated by the indirect mechanism, by at least a factor of 5.

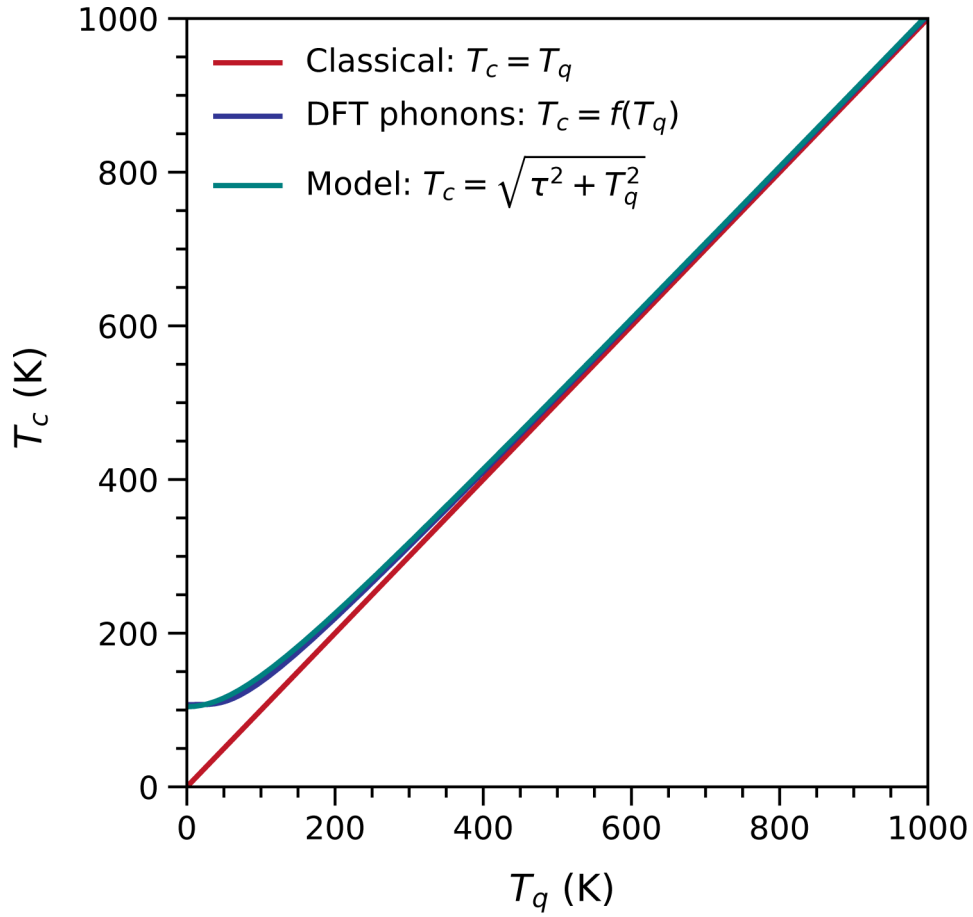

Extended Data Fig. 5 | The correspondence between the effective classical temperature T_c (our model) and the quantum (true) temperature T_q of perfect bulk bcc W. The classical, DFT phonons and our model are shown in red, dark blue and light blue respectively.